Assessment of Surface Exchange Coefficients in the Noah-MP Land Surface Model for Different Land Cover Types over China

Xia Zhang[1,2], Liang Chen[1,*], Zhuguo Ma[1,2], and **Yanhong Gao[3]**

[1]Key Laboratory of Regional Climate–Environment Research for Temperate East Asia, Institute of Atmospheric Physics, Chinese Academy of Sciences, Beijing, China,

[2]University of Chinese Academy of Sciences, Beijing, China,

[3]Key Laboratory of Land Surface Process and Climate Change in Cold and Arid Regions, Northwest Institute of Eco-Environment and Resources, Chinese Academy of Sciences, Lanzhou, China

[*]Corresponding author: Liang Chen (chenliang@tea.ac.cn)

Key Points:

- Impacts of C_{zil} on coupling strength as well as surface energy and water components over China were simulated
- The dynamic canopy-height-dependent C_{zil} scheme was found superior in reproducing observations
- The dynamic scheme performed better for short vegetation because of the treatment of the roughness length for heat

Abstract

The parameterization of surface exchange coefficients (C_h) representing land–atmosphere coupling strength plays a key role in land surface modeling. Previous studies have found that land–atmosphere coupling in land surface models (LSMs) is overestimated, which affects the predictability of weather and climate evolution. To improve the representation of land–atmosphere interactions in LSMs, this study investigated the dynamic canopy-height-dependent coupling strength in the offline Noah LSM with multiparameterization options (Noah-MP) when applied to China. Comparison with the default Noah-MP LSM showed the dynamic scheme significantly improved the C_h calculations and realistically reduced the biases of simulated surface energy and water components against observations. It is noteworthy that the improvements brought by the dynamic scheme differed across land cover types. The scheme was found superior in reproducing the observed C_h as well as surface energy and water variables for short vegetation (grass, crop, and shrub), while the improvement for tall canopy (forest) was found not significant, although the estimations were reasonable. The improved version benefits from the treatment of the roughness length for heat. Overall, the dynamic coupling scheme markedly affects the simulation of land–atmosphere interactions, and altering the dynamics of surface coupling has potential for improving the representation of land–atmosphere interactions and thus furthering LSM development.

Keywords: land–atmosphere interaction; surface coupling strength; surface exchange coefficient; surface fluxes

1. Introduction

Land–atmosphere interactions that are manifest as the exchange of energy, mass, and momentum between the land surface and the atmosphere play a fundamental role in the evolution of weather and climate systems (Betts et al., 1996; Knist et al., 2017; Los et al., 2006; Mahmood & Hubbard, 2003). Recent studies have shown that excessive land–atmosphere coupling in numerical models leads to large uncertainties regarding surface energy and water components. For example, Koster et al. (2004) identified several "hot spots" in terms of strong coupling between soil moisture (SM) and rainfall, some of which could not be captured correctly in the Global Land–Atmosphere Coupling Experiment study (Dirmeyer et al., 2006) or even did not register as regions of strong land–atmosphere coupling, e.g., the U.S. Southern Great Plains (Zhang et al., 2008). Relevant studies have been restricted by many factors such as the treatment of the roughness length for heat in land surface parameterizations (Chen et al., 1997; Chen & Zhang, 2009; LeMone et al., 2008) and the accuracy of the meteorological inputs (Santanello et al., 2009). Such work has highlighted the critical importance of models in predicting the strength of land–atmosphere coupling, as expressed by the surface exchange coefficients (C_h), although such fundamental coupling remains poorly understood.

The efficiencies of the exchange of energy and water vapor between the land surface and the lower atmosphere are represented by the parameter C_h. In a land surface model (LSM), this parameter controls the land–atmosphere coupling strength for different land cover types and climate regimes (Garratt, 1992; LeMone et al., 2008), which has consequences regarding the prediction of atmospheric, hydrological, and ecological components (LeMone et al., 2008; Li et al., 2009; Yang et al., 2011). The Noah LSM with multiparameterization options (Noah-MP) is a state-of-the-art LSM (Niu et al., 2011; Yang et al., 2011) that is used as an augmented land–surface scheme for the atmospheric Weather Research and Forecasting model (Barlage et al., 2015; Skamarock et al., 2008). Two C_h calculations provided in the Noah-MP LSM are the

Monin–Obukhov (M-O) (Brutsaert, 1982) and Chen97 (Chen et al., 1997) schemes, both of which are obtained through the M-O similarity theory and are mainly dependent on the roughness length for heat or moisture (Z_{ot}) and momentum (Z_{om}) as well as the atmospheric stability. The Chen97 scheme accounts for the difference between Z_{ot} and Z_{om} but not for zero-displacement height, while the M-O scheme is the opposite. The differences lead to the M-O scheme theoretically producing greater C_h and hence larger sensible heat flux (SH) than Chen97 (Niu et al., 2011). Recently, studies have indicated some deficiencies of the two schemes in their representation of land surface processes. For example, the M-O scheme stimulates more runoff than the Chen97 scheme, which is more consistent with observations (Yang et al., 2011). Moreover, Pilotto et al. (2015) found that using the M-O scheme produces surface fluxes and runoff with significant errors for an Amazonia forest site. However, the M-O scheme markedly improves the simulation of the land skin temperature, while Chen97 shows significant cold bias in arid regions of the western U.S. (Niu et al., 2011). The discrepancies are mainly attributed to the treatment of Z_{ot}/Z_{om} (Chen et al., 1997; Chen & Zhang, 2009). The parameter Z_{ot} is different from Z_{om} because heat and momentum transfers are determined by different resistances and mechanisms within the roughness layer (Chen & Zhang, 2009; Sun & Mahrt, 1995). The Z_{ot}/Z_{om} ratio can modulate surface fluxes through the change of an empirical coefficient C_{zil} (Zilitinkevich, 1995). Although the Chen97 scheme considers the differences between Z_{ot} and Z_{om}, a constant C_{zil} (usually specified as 0.1) is adopted in the C_h calculation of the scheme. However, studies have shown that C_{zil} values are dependent on vegetation type and that a dynamic C_{zil} could be more appropriate for reducing the impact of land–atmosphere coupling strength on surface fluxes (Chen & Zhang, 2009; Zheng et al., 2015). These earlier studies have shown the great potential for improvement in model performance through implementation of a dynamic C_{zil} in the M-O scheme that accounts for zero-displacement height, which is not considered in the Chen97 scheme (Yang et al., 2011).

Chen et al. (2019) assessed the effect of a dynamic C_{zil} on surface heat flux, temperature, and precipitation at eight FLUXNET Canada sites and seven AmeriFlux sites. However, the impact of land–atmosphere coupling within LSMs with regard to China has yet to be clarified because of the complexity of climate change, terrain, and vegetation distribution as well as the lack of observations. In the current study, we extended that modeling and analysis method using data collected from nine ChinaFlux sites and obtained from the China Meteorological Administration. Using the offline Noah-MP LSM, the objective of this study is to evaluate the impact of C_{zil} in the M-O scheme on land–atmosphere coupling strength as well as on surface energy and water components over China. Section 2 describes the experimental setup of the offline Noah-MP LSM and provides details of the land–atmosphere coupling method. Section 3 focuses on evaluation of the simulation results against observations in terms of coupling strength as well as surface energy and water components. Discussions and conclusions are provided in sections 4 and 5, respectively.

2. Data and Methods

2.1. Land–Atmosphere Coupling Method

LSMs can provide SH and surface latent heat flux (LH), as lower-boundary-layer conditions for coupled atmospheric models, to control the diurnal evolution and stability of the planetary boundary layer and subsequently to affect the development of weather and climate (Liu et al., 2017; Trier et al., 2011). SH and LH are determined through the bulk transfer relations (Garratt, 1992) as:

$$SH = \rho C_p C_h |U|(\theta_s - \theta_a) \quad (1)$$

$$LH = \rho C_e |U|(q_s - q_a) \quad (2)$$

$$C_h = \frac{SH}{\rho C_p |U|(\theta_s - \theta_a)} \quad (3)$$

where ρ is the air density, C_p is the heat capacity of air, and U is the wind speed. Here, C_h and C_e are the surface exchange coefficients of SH and LH, respectively. Generally, C_e is assumed equal to C_h, which controls the total surface heat flux input

into the atmosphere and can be associated directly with the coupling strength; therefore, we hereafter focus on C_h. In the above equations, θ_a and q_a represent the potential temperature and specific humidity of the air at the lowest model level or at a specific measurement height above the ground, and θ_s and q_s are the surface potential temperature and specific humidity. In addition, the observed C_h can be reconstituted from the observations of variables contained in Eq. (3) transformed from Eq. (1) (Chen & Zhang, 2009). Instruments at observing stations can provide direct measurements of *SH* and *U*, whereas θ_a is calculated from observed air temperature adjusted adiabatically for height above the surface, and θ_s is converted from downward and upward longwave radiation with the surface emissivity derived from observations (Yang et al., 2008). The values of C_p and ρ are derived from air temperature, relative humidity, and precipitation.

Within the Noah-MP LSM, C_h for the M-O scheme is computed based on the M-O similarity theory (Brutsaert, 1982) as:

$$C_h = \frac{k^2}{\left[\ln\left(\frac{z-d_0}{z_{om}}\right)-\psi_m\left(\frac{z-d_0}{L}\right)\right]\left[\ln\left(\frac{z-d_0}{z_{ot}}\right)-\psi_h\left(\frac{z-d_0}{L}\right)\right]} \quad (4)$$

where L is the M-O length, k is the von Kármán constant (=0.4), d_0 is the zero-displacement height, Ψ_m and Ψ_h are stability functions, Z is the height above the ground surface, Z_{om} is the roughness length for momentum, and Z_{ot} is the roughness length for moisture and heat. The parameter Z_{om} represents the height at which the average wind goes to zero and the scalars at $Z < Z_{om}$ are assumed transported by molecular processes. The parameter Z_{ot} is the height at which the air temperature is equal to the soil surface temperature.

In the Noah-MP LSM, Z_{ot} is related to Z_{om} as a function of atmospheric flow, as proposed by Zilitinkevich (1995):

$$Z_{ot} = Z_{om}\exp\left(-kC_{zil}\sqrt{R_e}\right), \quad R_e = \frac{u_0^* Z_{om}}{\upsilon} \quad (5)$$

where C_{zil} is an empirical coefficient, R_e is the roughness Reynolds number, u_0^* is the friction velocity, and υ is the kinematic molecular viscosity. The C_{zil} values are

assumed to vary from 0.01 to 1.00, denoting strong to weak surface coupling (Chen et al., 1997; Zheng et al., 2015). The value of C_{zil} is usually specified as 0.1, which is based on calibration with field data measured over grassland (Chen et al., 1997).

Smaller values of C_{zil} generate larger Z_{ot}, which indicates a rougher surface for heat and moisture, resulting in stronger turbulence and larger C_h. The adjustment of C_{zil} can contribute to improved model estimates of surface fluxes (Gutmann & Small, 2007; LeMone et al., 2008; Moncrieff, 2004). Furthermore, using the least squares regression method, Chen and Zhang (2009) analyzed multiyear Ameriflux data to determine that C_{zil} values are dependent on vegetation type and can be represented as a function of canopy height h (unit: m):

$$C_{zil} = 10^{(-0.4h)} \quad (6)$$

The primary focus of this study was implementation of the formula for the canopy-height-dependent C_{zil} into the M-O scheme to assess its impact on the simulations.

2.2. Offline Noah-MP LSM and Modeling Setting

The Noah-MP LSM has been developed to improve the performance of the Noah LSM (Chen & Dudhia, 2001; Chen et al., 1996), and it provides a multiparameterization framework that allows different combinations of available land process schemes (Niu et al., 2011; Yang et al., 2011). In this study, the Noah-MP LSM v3.6 was used in an offline standalone mode to execute single-site and regional-scale land surface experiments. Single-point experiments were executed at nine flux tower sites (Figure 1 and Table 1), while the simulated regional domain covered all of China (Figure 1). The atmospheric forcing fields used in the Noah-MP LSM were wind speed, air temperature, relative humidity, air pressure, precipitation, and downward shortwave and longwave radiation. Single-point experiments were forced by 30-min ChinaFlux observations; regional experiments were forced by the Global Land Data Assimilation System (GLDAS2.1) product with temporal and spatial resolutions of 3 h and 0.25°, respectively, during 2003–2012 (Rodell et al.,

2004). Regional simulations were initialized using the land use, soil texture, terrain height, and land–water mask through the preprocessing system of the Weather Research and Forecasting model. The Noah-MP physics options used in the study are listed in Table 2.

Three cases were designed to simulate the different responses of coupling strength as well as the surface water and energy components to C_{zil} in the M-O scheme: (1) the original M-O option with identical Z_{om} and Z_{ot} (Default), (2) a constant C_{zil} specified as 0.1 (C_{zil} = 0.1 or Czil), and (3) a dynamic canopy-height-dependent C_{zil} (C_{zil}-h or Newczil). In these simulations, everything was identical except for the surface-layer parameterization scheme.

To initialize the Noah-MP LSM properly, we first examined the spin-up time required to reach the equilibrium stage, defined as when the difference between two consecutive one-year simulations becomes <0.1% for the annual means (Cai et al., 2014; Chen et al., 2016; Yang et al., 1995). Almost all sites required no more than 9 years to reach equilibrium, except site Sw2 (at least 13 years). Areas with sparse vegetation and deep soil layers usually require a long time to reach equilibrium, which was true of Sw2 being the driest of the nine sites (Chen & Mitchell, 1999; Cosgrove et al., 2003). Consequently, we ran a 10-year spin-up initialization for all stations except Sw2 (20 years) for the single-point experiments, and we conducted 20-year-long runs as spin-up for the regional experiments.

2.3. Validation Datasets

The ChinaFlux network provides observations at 30-min intervals at nine flux tower sites located in areas with different land cover types (grassland, forest, and wetland) and climatic regimes (arid, wet, semiarid, and semihumid regions). Figure 1 shows the geographical locations of the nine ChinaFlux network sites and associated general information is presented in Table 1. Surface energy and water variables in the observations were used for evaluation of the LSM outputs in addition to forcing the Noah-MP single-point experiments. Several missing data for relative humidity and net

surface radiation were gap-filled using the nearby observations.

Regional C_h was calculated using surface monthly meteorological data (V3.0) obtained from the China Meteorological Administration. These data comprised monthly air temperature, wind speed, relative humidity, pressure, and ground surface temperature obtained at over 2000 stations during 2003–2012. We interpolated these monthly site observations to 0.25° spatial resolution using a Cressman-type interpolation. Regional-scale surface energy fluxes simulated by the Noah-MP LSM were validated using observation-based FLUXNET-MTE (Model Tree Ensemble) data. The gridded FLUXNET-MTE dataset, with monthly temporal resolution and 0.0833° spatial resolution, was integrated with observations from global 253 FLUXNET eddy covariance towers using machine learning technology, i.e., the MTE algorithm (Jung et al., 2009). We resampled the products from 0.0833° to 0.25° using a bilinear interpolation method. The gridded dataset was incomplete over western China because of the lack of in situ observations. Moreover, the uncertainty in the FLUXNET-MTE product owing to the uneven spatial distribution of flux towers selected for training the model tree is not negligible.

2.4. Evaluation Statistics

The level of agreement between model simulations and field observations is usually measured via three statistics (Brovkin et al., 2013; Dai et al., 2019; Frydrychowicz-Jastrzebska & Bugala, 2015): the Pearson correlation coefficient (R), root mean square error (RMSE), and mean bias error (MBE):

$$\mathrm{R} = \frac{\sum_{i=1}^{N}(M_i-\bar{M})\,(O_i-\bar{O})}{\sqrt{\sum_{i=1}^{N}(M_i-\bar{M})^2}\sqrt{\sum_{i=1}^{N}(O_i-\bar{O})^2}} \tag{7}$$

$$\mathrm{MBE} = \frac{1}{N}\sum_{i=1}^{N}(M_i - O_i) \tag{8}$$

$$\mathrm{RMSE} = \sqrt{\frac{\sum_{i=1}^{N}(M_i-O_i)^2}{N}} \tag{9}$$

where M_i and O_i are the model simulated and field observed values for the same variable, respectively, $\bar{M}$ and $\bar{O}$ are the means of the simulations and observations, respectively, and N is the number of days.

3. Model Verification and Comparisons

To explore the sensitivity of land–atmosphere coupling strength to C_{zil}, and to determine whether the C_{zil}-h scheme could improve climate simulations, three C_{zil} schemes (the default M-O, C_{zil} = 0.1, and C_{zil}-h) were implemented in the Noah-MP LSM and evaluated for different land cover types over China. First, we compared the performance of each scheme in quantifying the land–atmosphere coupling strength against the observed C_h, and then we assessed the impact on the surface energy and water components.

3.1. Surface Coupling Strength Sensibility to C_{zil}

Because the representation of C_{zil} realized by varying the degrees of surface exchange simulation significantly affects the evolution of weather and climate systems (Chen & Zhang, 2009; LeMone et al., 2008; Trier et al., 2011), we first analyzed the impact of each C_{zil} scheme on its C_h calculation. Figure 2 compares the observations and simulations of the midday C_h averaged from 10:00–15:00 local time for the nine ChinaFlux sites in spring and summer, i.e., during the growth season of vegetation. Compared with the observation-derived C_h, the C_h values modeled by the Noah-MP LSM have much smaller variability and seasonality across the various land cover types. Boreal sites (such as Cng) experience a large increase in summer C_h as the land cover changes from a smooth sparsely vegetated surface in spring to a rougher surface with flourishing vegetation in summer, as reflected clearly by the observed C_h. The simulated C_h values based on the default M-O scheme are substantially overestimated at almost all sites, especially in grassland areas. The C_h values simulated in the C_{zil} = 0.1 experiment are decreased, but the unsatisfactory reduction results in insufficient underestimation at grassland sites and slightly too efficient underestimation for forest

sites. In comparison, the C_h values derived from the C_{zil}-h scheme are in better agreement with the observations, especially sites with short vegetation (such as grass), suggesting significant improvement in the performance of the C_{zil}-h scheme in comparison with the other two in terms of the representation of the land–atmosphere coupling strength. Additionally, the C_{zil}-h scheme provides reasonable estimations, similar to the default M-O scheme, at sites with tall vegetation (such as forest), although the overestimated C_h values against the observations, which are consistent with results over North America (Chen et al., 2019; Chen & Zhang, 2009), indicate similar skill of the C_{zil}-h scheme in terms of global applicability.

To confirm the findings obtained from the single-site simulations, long-term regional climate modeling over China was conducted to further examine the climatological behavior of land–atmosphere coupling strength sensibility to C_{zil}. Figure 3 shows the observed and Noah-MP modeled C_h over China during the summers of 2003–2012. Spatial climatology differences between the observations and the simulations of the three C_{zil} schemes are shown in Figure 3a–c. Compared with the observations, the C_h values of the default M-O scheme are substantially overestimated with too efficient coupling, while the C_{zil} = 0.1 scheme slightly modulates the positive deviation. In contrast, the C_{zil}-h scheme presents the smallest bias against the observations for short vegetation types (grass, crop, and shrub), and it produces overestimated but reasonable C_h values for sites with tall vegetation (forest) in comparison with the default run, with similar results for the nine ChinaFlux sites. Spatial differences between the C_{zil} schemes (Figure 3d and 3e) also show that both the C_{zil} = 0.1 and the C_{zil}-h schemes present negative bias against the default run in most parts of China. Additionally, the spatial patterns of the differences are similar to that of vegetation canopy height, implied by a significant boundary between short and tall canopy, for either the C_{zil} = 0.1 scheme or the C_{zil}-h scheme. These findings indicate that the C_h values are more realistically related to the canopy-height-dependent C_{zil}. From the perspective of vegetation type, we further quantified the sensitivity of the coupling

strength response to C_{zil} for different land cover types, as shown in Figure 3f. For barren land or sparse vegetation, crop, grass, and shrub, the regional average C_h values modeled by the C_{zil}-*h* run are the smallest in terms of three C_{zil} experiments. In contrast, the default M-O scheme obtains overly high estimates, while the C_{zil}-*h* simulations for forest are similar to the default run.

3.2. Surface Energy and Water Variations Affected by C_{zil}

The parameter C_h, representing the exchange efficiency between land and atmosphere, plays an important role in controlling surface energy and water variables in the Noah-MP LSM (Yang et al., 2011). The values of C_h simulated by the C_{zil}-*h* scheme have been verified to be closer to the observations compared with the other two schemes. Therefore, we further evaluated the potential skill of the three C_{zil} schemes incorporated into the Noah-MP LSM in reproducing the observed surface energy and water variables.

Figures 4–7 present the daily average soil temperature (ST) and SM at the depth of 0–10 cm, as well as SH and LH, at nine ChinaFlux sites (Dan, Sw2, Cng, HaM, Du2, Ha2, Qia, Din, and Cha; Table 1). The LSM shows the ability to favorably capture the seasonal variability of the surface energy and water variables. For each C_{zil} experiment, the simulations have significant correlations with the observations at the nine sites, and the minimum correlation coefficients passing the 95% confidence level for ST, SM, SH, and LH are 0.96 (Ha2), 0.38 (Cha), 0.32 (HaM), and 0.81 (Din), respectively. All these results demonstrate that the Noah-MP LSM has good performance with regard to the surface energy and water variables at these sites. Comparisons of the simulated and observed ST at the nine stations are shown in Figure 4 and Table 3. Generally, the values of ST are all underestimated by the three C_{zil} schemes in comparison with the observations. However, the C_{zil}-*h* scheme presents its superiority over the default M-O scheme and the C_{zil} = 0.1 scheme at most sites. The C_{zil}-*h* scheme shows greater consistency between the simulation and the observations, as revealed by the smallest RMSE at five of the nine sites (Dan, HaM,

Qia, Din, and Cha), as well as the highest correlation at six sites (Dan, Sw2, Du2, Qia, Din, and Cha). The cold season ST values are substantially underestimated by all three C_{zil} schemes, while the C_{zil}-h scheme slightly modulates the negative deviations. The daily mean simulated SM values against the observations are shown in Figure 5 and Table 4. Precipitation is a key contributor to the seasonal variability of SM. Usually, SM exhibits large daily variations during summer when most rainfall events are concentrated, while SM fluctuations are stable during winter when fewer rainfall events take place. The three C_{zil} schemes capture the seasonal evolutions of SM reasonably well. There are dry biases at Sw2, Cng, HaM, and Cha, while the remaining sites have wet biases. Similarly, the C_{zil}-h scheme slightly narrows the discrepancy of the simulation from the observations, with the smallest RMSE at seven of the nine sites. Figures 6 and 7 show daily averaged SH and LH variations, respectively. Simulated SH shows positive biases against the observations for most sites (Table 5), while LH shows negative values (Table 6). Compared with the other two schemes, the C_{zil}-h scheme shows values of SH and LH that are more comparable with the observations, with the smallest RMSE at most stations.

At the regional scale, we analyzed the seasonally spatial differences of LH and SH modeled by the three C_{zil} experiments against FLUXNET-MTE observations, as Figure 8 shows. Overall, the surface energy fluxes simulated with a dynamical changing C_{zil} scheme show favorable spatial correspondence with FLUXNET-MTE data. Moreover, it should also be noted that the influence of C_{zil} on LH is smaller compared with SH, suggesting less spatial heterogeneity regarding the differences in the modeling simulations.

3.3. Impacts of C_{zil} on Short and Tall Canopy Types

We have thus far shown that the variability of C_h across land cover types becomes clear and that it can be divided roughly into short (grass, crop, and shrub) and tall (forest) vegetation categories in order of increasing C_h. Therefore, from the

perspective of canopy types, we hereafter address the effect of C_{zil} on the simulations in terms of on-site grassland (short canopy) and forest (tall canopy).

Synthetically considering the correlation coefficients and normalized standard deviations (Figure 9), the C_{zil}-*h* experiments show that the majority of short vegetation sites present significant improvements in the simulations, i.e., the C_{zil}-*h* simulations closest to the observations occur at three of five sites (Sw2, HaM, and Du2) for LH, at four sites (Dan, Sw2, Cng, and Du2) for SH, and at three sites (Dan, Cng, and HaM) for SM. Regarding three tall vegetation sites (Qia, Din, and Cha), the C_{zil}-*h* scheme shows the same level of ability as the default M-O in simulating the surface energy and water components.

Diurnal surface heat fluxes for short and tall vegetation are shown in Figure 10. The simulations for short vegetation are averages from five ChinaFlux grassland sites (Dan, Sw2, Cng, HaM, and Du2), while those for tall vegetation are averages from three forest sites (Qia, Din, and Cha). The modeled LH values show negligible differences among the three C_{zil} schemes for both short and tall canopy types, but underestimations (overestimations) are evident against the observed LH for short (tall) canopy types. Comparatively, large discrepancies are found regarding the SH values simulated by the different C_{zil} schemes, especially around midday (10:00–15:00 local time). In comparison with the observed SH at grassland sites, the default M-O run overestimates SH with coupling strength that is too strong, especially in summer; however, the C_{zil}-*h* simulations agree well with the observed SH but with underestimation in spring. For forest sites, the C_{zil}-*h* scheme produces the same level of variation in SH as the default M-O scheme, while the $C_{zil} = 0.1$ scheme simulates the smallest SH values.

4. Discussions

4.1. Superiority of the C_{zil}-h Scheme in Regenerating Observations across Land Cover Types

The default M-O scheme substantially overestimates the land–atmosphere coupling strength relative to the observations, which might illustrate a deficiency of LSMs, i.e., LSMs might have overly strong coupling that results in the transfer of too much energy and water vapor (Chen & Zhang, 2009; Ruiz-Barradas & Nigam, 2005). Correct determination of the coupling strength is closely related to the definition of the calculation of Z_{ot} in LSMs (Brutsaert, 1982; Garratt, 1992; Sun & Mahrt, 1995). The analysis in section 3 demonstrated that modest adjustment of the C_{zil} values affecting the treatment of Z_{ot} in Eq. (5) could significantly improve the land–atmosphere coupling strength. However, such impacts should be viewed across land cover types. Compared with the default M-O scheme of the Noah-MP LSM, the C_{zil}-h scheme provides significant improvements in the simulations for short vegetation; improvements for tall canopy types are not evident, although the estimations are reasonable, which is consistent with results obtained in North America (Chen et al., 2019; Chen & Zhang, 2009). Regarding the ability for direct connection between surface coupling strength and terrestrial ecosystems in Eq. (6), the C_{zil}-h scheme realistically reduces the coupling strength for short canopy types, but produces positive bias similar to that of the default M-O run for tall canopy types because of the equivalent heat and momentum roughness length resulting from a close-to-zero C_{zil}. Tall vegetation with a rough surface has large values of C_h, and hence generally stronger coupling, with C_h values 10 times larger than for shorter vegetation (Chen & Zhang, 2009). Regarding shorter canopy types, with increasing C_{zil}, the coupling strength becomes weak, resulting in less rough surface for heat or moisture transfer, and the simulated surface fluxes are less spatially heterogeneous. For the C_{zil}-h scheme, the smaller values of C_{zil} resulting from the taller canopy enhance the C_h values and hence the surface coupling strength; however, C_{zil} shows little change

when the canopy height is >5 m, as indicated by Eq. (6). For example, the difference in C_{zil} values between vegetation canopy heights of 1 and 2 m is 0.24, whereas it is only 1.51×10^{-8} between canopy heights of 19 and 20 m. As such, assigning different C_{zil} values for different land cover types will allow the Noah-MP LSM to reasonably reproduce the observed C_h. It should also be noted that the values of summer C_h are slightly larger than spring because of the rougher surface with vegetation greening from spring to summer. Therefore, in spring with the slightly weaker coupling strength in comparison with summer, the C_{zil}-h scheme is likely to produce overly low simulations, as shown in Figure 10a.

4.2. Discrepancy of C_{zil} Impacts on Surface Energy Partitioning

To understand how C_{zil} affects surface energy components, for instance, why the influence of C_{zil} on LH appears smaller than on SH (Figure 10), we tried to account for the issue from the perspective of the surface energy budget. Recent studies have shown that the surface energy balance problem is subject to many factors, such as measurement errors, heat storage in soil and canopy, as well as exchange processes on large scales of the heterogeneous landscape (Etchevers et al., 2004; Foken, 2008; Franssen et al., 2010; Tang et al., 2019). However, the available energy of net radiation and ground heat flux as well as the turbulent fluxes of sensible and latent heat are able to explain approximately 80% of the closure of the energy balance (Kanemasu et al., 1992; Leuning et al., 1982; Wilson et al., 2002). Therefore, here, the discrepancy of C_{zil} impacts on surface energy partitioning is considered in terms of available energy and turbulent fluxes. Net radiation not directly provided by LSM outputs can be derived as the residual of the radiation budget balance, i.e., the deficit between downward and upward radiation (Xin et al., 2018). Figure 11 shows the spatial relative differences between the C_{zil} schemes for SH, LH, ground heat flux, and net radiation. The simulated SH and ground heat flux differ markedly with the C_{zil} schemes, while the simulated net radiation appears insensitive to the C_{zil} values. For LH, the values tend to vary little with the different C_{zil} schemes, but marked

differences can be found between the C_{zil}-h and default schemes in spring. The C_{zil}-h experiment modeled smaller LH over eastern regions of China and larger values over most western and northeastern areas. The situation was reversed for SH. The C_{zil}-h scheme simulated smaller SH over much of China, leading to less heat being transported from the surface into the atmosphere; thus, an increase in surface temperature enhances ground heat flux.

5. Conclusions

The impact of land–atmosphere coupling within LSMs with regard to China has yet to be clarified because of the complexity of climate change, terrain, and vegetation distribution as well as the lack of observations. In this study, using observations collected from nine ChinaFlux sites and data from over 2000 automatic meteorological stations, the impacts of land–atmosphere coupling for different land cover types over China were assessed. This was achieved by testing three C_{zil} schemes (the default M-O, constant C_{zil} = 0.1, and dynamic canopy-height-dependent C_{zil}-h schemes) with the offline Noah-MP LSM. The parameter C_{zil} is strongly associated with C_h, which is a critical parameter in the transfer of surface energy into the lower atmosphere and directly reflects the land–atmosphere coupling strength. By performing both single-site and regional-scale experiments, we verified and compared the sensibility of C_h and subsequently of the surface energy and water components in response to different C_{zil} schemes. The main results of the study can be summarized as follows.

The different C_{zil} schemes have considerable impact on surface coupling strength. The default M-O scheme, which has equivalent roughness length for heat and momentum with no-C_{zil}, substantially overestimates C_h. The constant C_{zil} = 0.1 scheme reduces the positive C_h bias produced by the default scheme for short vegetation (grass, crop, and shrub); however, it overly underestimates C_h for tall vegetation (forest). In contrast, the C_{zil}-h scheme produces the least C_h bias against the observations for short

canopy types, and provides overestimated but reasonable values for tall canopy types, similar to the default M-O simulation.

The accuracy of simulated surface water and energy components in LSMs is closely related to surface coupling strength, which is in turn determined by C_{zil}. As the discrepancies in C_h produced by the different C_{zil} schemes show, in general, the C_{zil}-*h* scheme significantly reduces the bias against observations in comparison with the default and constant C_{zil} schemes. The C_{zil}-*h* scheme can better reproduce the observed surface energy components, while the improvement in water variables such as SM remains limited.

Assigning different C_{zil} values for different land cover types displays the superiority of the Noah-MP LSM in reproducing the observed C_h, as well as the surface variables for short vegetation (grass, crop, and shrub), while the improvement for the tall vegetation (forest) is not significant, although the estimation are reasonable. These results underline the critical importance of C_{zil} in relation to canopy height in LSMs, and thus raise other intriguing problems for further study, e.g., the question of how to effectively improve simulations for tall vegetation through optimization of the C_{zil}-*h* scheme, and how best to employ coupled climate models to investigate the effects of C_h on climate simulations.

Acknowledgments

This work was funded by the National Key Research and Development Program of China (grant number: 2016YFA0600403), National Natural Science Foundation of China (grant number: 41875116), and Open fund of the Key Laboratory of Land Surface Process and Climate Change in Cold Arid Area of the Chinese Academy of Sciences “Influence of land–atmosphere coupling intensity on regional climate in arid regions of Northwest China” (grant number: LPU2017001). The meteorological station data used in this study are available from the China Meteorological

Administration (http://data.cma.cn/). The ChinaFlux observation data are from the FLUXNET network (http://www.fluxdata.org), and the FLUXNET model tree ensembles (MTE) latent heat flux and sensible heat flux data are from the Max Planck Institute for Biogeochemistry (http://www.bgc-jena.mpg.de/geodb/). Model output used is available at online (https://doi.org/10.5281/zenodo.3560864). There are no conflicts of interest.

References

Barlage, M., Tewari, M., Chen, F., Miguez-Macho, G., Yang, Z. L., & Niu, G. Y. (2015). The effect of groundwater interaction in North American regional climate simulations with WRF/Noah-MP. *Climatic Change, 129*(3-4), 485-498. doi:10.1007/s10584-014-1308-8.

Betts, A. K., Ball, J. H., Beljaars, A. C. M., Miller, M. J., & Viterbo, P. A. (1996). The land surface-atmosphere interaction: A review based on observational and global modeling perspectives. *Journal of Geophysical Research: Atmospheres, 101*(D3), 7209-7225. doi:10.1029/95jd02135.

Brovkin, V., Boysen, L., Raddatz, T., Gayler, V., Loew, A., & Claussen, M. (2013). Evaluation of vegetation cover and land-surface albedo in MPI-ESM CMIP5 simulations. *Journal of Advances in Modeling Earth Systems, 5*(1), 48-57. doi:10.1029/2012ms000169.

Brutsaert, W. A. (1982). *Evaporation into the atmosphere: Theory, history and applications* (pp. 299). D. Reidel, Dordrecht, Netherlands: Cornell University, USA. https://doi.org/10.1007/978-94-017-1497-6.

Cai, X. T., Yang, Z. L., David, C. H., Niu, G. Y., & Rodell, M. (2014). Hydrological evaluation of the Noah-MP land surface model for the Mississippi River Basin. *Journal of Geophysical Research-Atmospheres, 119*(1), 23-38. doi:10.1002/2013jd020792.

Chen, F., & Dudhia, J. (2001). Coupling an advanced land surface-hydrology model with the Penn State-NCAR MM5 modeling system. Part I: Model implementation and sensitivity. *Monthly Weather Review, 129*(4), 569-585. doi:10.1175/1520-0493(2001)129<0569:caalsh>2.0.co;2.

Chen, F., Janjic, Z., & Mitchell, K. (1997). Impact of atmospheric surface-layer parameterizations in the new land-surface scheme of the NCEP mesoscale Eta model. *Boundary-Layer Meteorology, 85*(3), 391-421. doi:10.1023/a:1000531001463.

Chen, F., & Mitchell, K. (1999). Using the GEWEX/ISLSCP forcing data to simulate global soil moisture fields and hydrological cycle for 1987-1988. *Journal of the Meteorological Society of Japan, 77*(1B), 167-182. doi:10.2151/jmsj1965.77.1B_167.

Chen, F., Mitchell, K., Schaake, J., Xue, Y. K., Pan, H. L., Koren, V., et al. (1996). Modeling of land surface evaporation by four schemes and comparison with FIFE observations. *Journal of Geophysical Research-Atmospheres, 101*(D3), 7251-7268. doi:10.1029/95jd02165.

Chen, F., & Zhang, Y. (2009). On the coupling strength between the land surface and the atmosphere: From viewpoint of surface exchange coefficients. *Geophysical Research Letters, 36*(10), 1-5. doi:10.1029/2009gl037980.

Chen, L., Li, Y. P., Chen, F., Barlage, M., Zhang, Z., & Li, Z. H. (2019). Using 4-km WRF CONUS simulations to assess impacts of the surface coupling strength on regional climate simulation. *Climate Dynamics, 53*(9-10), 6397-6416. doi:10.1007/s00382-019-04932-9.

Chen, L., Li, Y. P., Chen, F., Barr, A., Barlage, M., & Wan, B. C. (2016). The incorporation of an organic soil layer in the Noah-MP land surface model and its evaluation over a boreal aspen forest. *Atmospheric Chemistry and Physics, 16*(13), 8375-8387. doi:10.5194/acp-16-8375-2016.

Cosgrove, B. A., Lohmann, D., Mitchell, K. E., Houser, P. R., Wood, E. F., Schaake, J. C., et al. (2003). Real-time and retrospective forcing in the North American Land Data Assimilation System (NLDAS) project. *Journal of Geophysical Research-Atmospheres, 108*(D22), 1-12. doi:10.1029/2002jd003118.

Dai, Y. J., Xin, Q. C., Wei, N., Zhang, Y. G., Wei, S. G., Yuan, H., et al. (2019). A Global High-Resolution Data Set of Soil Hydraulic and Thermal Properties for Land Surface Modeling. *Journal of Advances in Modeling Earth Systems, 11*(9), 2996-3023. doi:10.1029/2019ms001784.

Dirmeyer, P. A., Koster, R. D., & Guo, Z. C. (2006). Do global models properly represent the feedback between land and atmosphere? *Journal of Hydrometeorology, 7*(6), 1177-1198. doi:10.1175/jhm532.1.

Etchevers, P., Martin, E., Brown, R., Fierz, C., Lejeune, Y., Bazile, E., et al. (2004). Validation of the energy budget of an alpine snowpacksimulated by several snow models (Snow MIP project). *Annals of Glaciology, 38*, 150–158. https://doi.org/10.3189/172756404781814825

Foken, T. (2008). The energy balance closure problem: An overview. *Ecological Applications, 18*(6), 1351-1367. doi:10.1890/06-0922.1.

Franssen, H. J. H., Stockli, R., Lehner, I., Rotenberg, E., & Seneviratne, S. I. (2010). Energy balance closure of eddy-covariance data: A multisite analysis for European FLUXNET stations. *Agricultural and Forest Meteorology, 150*(12), 1553-1567. doi:10.1016/j.agrformet.2010.08.005.

Frydrychowicz-Jastrzebska, G., & Bugala, A. (2015). Modeling the Distribution of Solar Radiation on a Two-Axis Tracking Plane for Photovoltaic Conversion. *Energies, 8*(2), 1025-1041. doi:10.3390/en8021025.

Garratt, J. R. (1992). The atmospheric boundary layer (pp. 316). Cambridge University Press, New York.

570 Gutmann, E. D., & Small, E. E. (2007). A comparison of land surface model soil
571 hydraulic properties estimated by inverse modeling and pedotransfer functions.
572 *Water Resources Research, 43*(5), 1-13. doi:10.1029/2006wr005135.
573 Jung, M., Reichstein, M., & Bondeau, A. (2009). Towards global empirical upscaling
574 of FLUXNET eddy covariance observations: validation of a model tree ensemble
575 approach using a biosphere model. *Biogeosciences, 6*(10), 2001-2013.
576 doi:10.5194/bg-6-2001-2009.
577 Kanemasu, E. T., Verma, S. B., Smith, E. A., Fritschen, L. J., Wesely, M., Field, R. T.,
578 et al. (1992). Surface flux measurements in FIFE: An overview. *Journal of*
579 *Geophysical Research-Atmospheres, 97*(D17), 18547-18555.
580 doi:10.1029/92jd00254.
581 Knist, S., Goergen, K., Buonomo, E., Christensen, O. B., Colette, A., Cardoso, R. M.,
582 et al. (2017). Land-atmosphere coupling in EURO-CORDEX evaluation
583 experiments. *Journal of Geophysical Research-Atmospheres, 122*(1), 79-103.
584 doi:10.1002/2016jd025476.
585 Koster, R. D., Dirmeyer, P. A., Guo, Z. C., Bonan, G., Chan, E., Cox, P., et al. (2004).
586 Regions of strong coupling between soil moisture and precipitation. *Science,*
587 *305*(5687), 1138-1140. doi:10.1126/science.1100217.
588 LeMone, M. A., Tewari, M., Chen, F., Alfieri, J. G., & Niyogi, D. (2008). Evaluation
589 of the Noah Land Surface Model Using Data from a Fair-Weather IHOP_2002
590 Day with Heterogeneous Surface Fluxes. *Monthly Weather Review, 136*(12),
591 4915-4941. doi:10.1175/2008mwr2354.1.
592 Leuning, R., Denmead, O. T., Lang, A. R. G., & Ohtaki, E. (1982). Effects of heat and
593 water-vapor transport on eddy covariance measurement of co2 fluxes.
594 *Boundary-Layer Meteorology, 23*(2), 209-222. doi:10.1007/bf00123298.
595 Li, Z., Liu, W. Z., Zhang, X. C., & Zheng, F. L. (2009). Impacts of land use change
596 and climate variability on hydrology in an agricultural catchment on the Loess

Plateau of China. *Journal of Hydrology, 377*(1-2), 35-42. doi:10.1016/j.jhydrol.2009.08.007.

Liu, C. H., Ikeda, K., Rasmussen, R., Barlage, M., Newman, A. J., Prein, A. F., et al. (2017). Continental-scale convection-permitting modeling of the current and future climate of North America. *Climate Dynamics, 49*(1-2), 71-95. doi:10.1007/s00382-016-3327-9.

Los, S. O., Weedon, G. P., North, P. R. J., Kaduk, J. D., Taylor, C. M., & Cox, P. M. (2006). An observation-based estimate of the strength of rainfall-vegetation interactions in the Sahel. *Geophysical Research Letters, 33*(16), 5. doi:10.1029/2006gl027065.

Mahmood, R., & Hubbard, K. G. (2003). Simulating sensitivity of soil moisture and evapotranspiration under heterogeneous soils and land uses. *Journal of Hydrology, 280*(1-4), 72-90. doi:10.1016/s0022-1694(03)00183-5.

Moncrieff, M. W. (2004). Analytic representation of the large-scale organization of tropical convection. *Journal of the Atmospheric Sciences, 61*(13), 1521-1538. doi:10.1175/1520-0469(2004)061<1521:arotlo>2.0.co;2.

Niu, G. Y., Yang, Z. L., Mitchell, K. E., Chen, F., Ek, M. B., Barlage, M., et al. (2011). The community Noah land surface model with multiparameterization options (Noah-MP): 1. Model description and evaluation with local-scale measurements. *Journal of Geophysical Research-Atmospheres, 116*, 1-19. doi:10.1029/2010jd015139.

Pilotto, I. L., Rodriguez, D. A., Tomasella, J., Sampaio, G., & Chou, S. C. (2015). Comparisons of the Noah-MP land surface model simulations with measurements of forest and crop sites in Amazonia. *Meteorology and Atmospheric Physics, 127*(6), 711-723. doi:10.1007/s00703-015-0399-8.

Rodell, M., Houser, P. R., Jambor, U., Gottschalck, J., Mitchell, K., Meng, C. J., et al. (2004). The global land data assimilation system. *Bulletin of the American Meteorological Society, 85*(3), 381-+. doi:10.1175/bams-85-3-381.

Ruiz-Barradas, A., & Nigam, S. (2005). Warm season rainfall variability over the US great plains in observations, NCEP and ERA-40 reanalyses, and NCAR and NASA atmospheric model simulations. *Journal of Climate, 18*(11), 1808-1830. doi:10.1175/jcli3343.1.

Santanello, J. A., Peters-Lidard, C. D., Kumar, S. V., Alonge, C., & Tao, W. K. (2009). A Modeling and Observational Framework for Diagnosing Local Land-Atmosphere Coupling on Diurnal Time Scales. *Journal of Hydrometeorology, 10*(3), 577-599. doi:10.1175/2009jhm1066.1.

Skamarock, W.C., Klemp, J. B., Dudhia, J., Gill, D. O., Barker, D. M., Duda, M. G., et al. (2008). A description of the Advanced ResearchWRF version 3. NCAR Technical Notes, NCAR/TN‐4751STR.

Sun, J. L., & Mahrt, L. (1995). Determination of surface fluxes from the surface radiative temperature. *Journal of the Atmospheric Sciences, 52*(8), 1096-1106. doi:10.1175/1520-0469(1995)052<1096:dosfft>2.0.co;2.

Tang, S. Q., Xie, S. C., Zhang, M. H., Tang, Q., Zhang, Y. Y., Klein, S. A., et al. (2019). Differences in Eddy-Correlation and Energy-Balance Surface Turbulent Heat Flux Measurements and Their Impacts on the Large-Scale Forcing Fields at the ARM SGP Site. *Journal of Geophysical Research-Atmospheres, 124*(6), 3301-3318. doi:10.1029/2018jd029689.

Trier, S. B., LeMone, M. A., Chen, F., & Manning, K. W. (2011). Effects of Surface Heat and Moisture Exchange on ARW-WRF Warm-Season Precipitation Forecasts over the Central United States. *Weather and Forecasting, 26*(1), 3-25. doi:10.1175/2010waf2222426.1.

Wilson, K., Goldstein, A., Falge, E., Aubinet, M., Baldocchi, D., Berbigier, P., et al. (2002). Energy balance closure at FLUXNET sites. *Agricultural and Forest Meteorology, 113*(1-4), 223-243. doi:10.1016/s0168-1923(02)00109-0.

Xin, Y. F., Chen, F., Zhao, P., Barlage, M., Blanken, P., Chen, Y. L., et al. (2018). Surface energy balance closure at ten sites over the Tibetan plateau. *Agricultural and Forest Meteorology, 259*, 317-328. doi:10.1016/j.agrformet.2018.05.007.

Yang, K., Koike, T., Ishikawa, H., Kim, J., Li, X., Liu, H. Z., et al. (2008). Turbulent flux transfer over bare-soil surfaces: Characteristics and parameterization. *Journal of Applied Meteorology and Climatology, 47*(1), 276-290. doi:10.1175/2007jamc1547.1.

Yang, Z. L., Dickinson, R. E., Henderson-Sellers, A., & Pitman, A. J. (1995). Preliminary-study of spin-up processes in land-surface models with the first stage data of project for intercomparison of land-surface parameterization schemes phase 1(a). *Journal of Geophysical Research-Atmospheres, 100*(D8), 16553-16578. doi:10.1029/95jd01076.

Yang, Z. L., Niu, G. Y., Mitchell, K. E., Chen, F., Ek, M. B., Barlage, M., et al. (2011). The community Noah land surface model with multiparameterization options (Noah-MP): 2. Evaluation over global river basins. *Journal of Geophysical Research-Atmospheres, 116*, 1-16. doi:10.1029/2010jd015140.

Zhang, J. Y., Wang, W. C., & Leung, L. R. (2008). Contribution of land-atmosphere coupling to summer climate variability over the contiguous United States. *Journal of Geophysical Research-Atmospheres, 113*, 1-15. doi:10.1029/2008jd010136.

Zheng, Y., Kumar, A., & Niyogi, D. (2015). Impacts of land-atmosphere coupling on regional rainfall and convection. *Climate Dynamics, 44*(9-10), 2383-2409. doi:10.1007/s00382-014-2442-8.

Zilitinkevich, S. S. (1995). Non-local turbulent transport: Pollution dispersion aspects of coherent structure of convective flows. In H. Power, N. Moussiopoulos, & C. A. Brebbia (Eds.), *Air pollution III-volume I. Air pollution theory and simulation* (pp. 53–60). Southampton, Boston: Computational Mechanics Publications.

Table 1. General information regarding the nine FLUXNET sites.

Site Code	Site Name	Latitude, Longitude	Elevation (m)	Land-Cover Type	Canopy Height (m)	Years
CN-Dan	Dangxiong	30.50, 91.07	4250	GRA	0.1	2004-2005
CN-Sw2	Siziwang Banner	41.79, 111.90	1456	GRA	0.1~0.2	2011
CN-Cng	Changling	44.59, 123.51	270	GRA	0.17	2008
CN-HaM	Haibei Alpine	37.37, 101.18	3190	GRA	0.25	2003
CN-Du2	Duolun	42.05, 116.28	1324	GRA	0.3	2007
CN-Ha2	Haibei Shrubland	37.61, 101.33	3190	WET	0.6–0.7	2003-2005
CN-Qia	Qianyanzhou	26.74, 115.06	100	ENF	12	2003-2005
CN-Din	Dinghushan	23.17, 112.54	240	EBF	17	2003-2005
CN-Cha	Changbaishan	42.40, 128.10	738	MF	26	2003-2005

GRA: grasslands; WET: permanent wetlands; ENF: evergreen needleleaf forest; EBF: evergreen broadleaf forest; MF: mixed forests

Table 2. Noah-MP LSM parameterization options used in this study.

Parameterization description	Options
Dynamic vegetation	4: table LAI, shdfac=maximum
Stomatal resistance	1: BALL-Berry (Ball et al., 1987)
Soil moisture factor for stomatal resistance	1: original Noah (Chen and Dudhia, 2001)
Runoff/soil lower boundary	1: original surface and subsurface runoff (free drainage)
Surface layer drag coefficient calculation	1: Monin–Obukhov (Brutsaert, 1982)
Supercooled liquid water	1: no iteration (Niu and Yang, 2006)
Soil permeability	1: linear effects, more permeable (Niu and Yang, 2006)
Radiative transfer	3: two-stream applied to vegetated fraction
Surface albedo	2: CLASS (Verseghy, 1991)
Precipitation partitioning between snow and rain	1: Jordan (Jordan, 1991)
Soil temp lower boundary	2: TBOT at ZBOT (8 m) read from a file
Snow/soil temperature time	1: semi-implicit

Table 3. Statistics of daily averaged soil temperature at the depth of 0–10 cm from the nine FLUXNET sites. R, MBE, and RMSE denote the Pearson correlation coefficient, mean bias error, and root mean square error between the observation and simulation, respectively. Soil temperature simulated by the Noah-MP LSM using the default M-O scheme is represented by Default; using the C_{zil} = 0.1 scheme is represented by Czil; and using the C_{zil}-h scheme is represented by Newczil.

Site Code	Default			Czil			Newczil		
	R	MBE	RMSE	R	MBE	RMSE	R	MBE	RMSE
CN-Dan	0.98	-0.97	2.90	0.98	0.66	2.42	0.98	0.66	2.42
CN-Sw2	0.99	-3.47	21.30	0.99	-3.65	22.79	0.99	-3.44	23.90
CN-Cng	0.99	0.62	14.34	0.98	0.61	14.94	0.98	1.11	19.20
CN-HaM	0.97	-4.81	29.42	0.97	-4.66	28.32	0.97	-4.01	25.82
CN-Du2	0.99	-1.93	7.58	0.99	-1.80	7.39	0.99	-1.17	7.68
CN-Ha2	0.97	-2.54	10.89	0.97	-1.97	10.45	0.96	-1.07	16.29
CN-Qia	0.99	-0.47	3.22	0.99	0.46	4.39	0.99	-0.47	3.22
CN-Din	0.97	-0.09	2.99	0.97	0.70	3.67	0.97	-0.09	2.99
CN-Cha	0.97	-0.81	17.25	0.97	-0.22	21.12	0.97	-0.81	17.25

Table 4. As in Table 3 but for soil moisture at the depth of 0–10 cm.

Site Code	Default			Czil			Newczil		
	R	MBE	RMSE	R	MBE	RMSE	R	MBE	RMSE
CN-Dan	0.84	0.07	0.01	0.87	0.07	0.01	0.87	0.07	0.01
CN-Sw2	0.72	-0.01	0.002	0.72	-0.01	0.002	0.69	-0.01	0.002
CN-Cng	0.69	-0.13	0.04	0.69	-0.13	0.04	0.72	-0.13	0.04
CN-HaM	0.94	-0.13	0.02	0.94	-0.13	0.02	0.95	-0.13	0.02
CN-Du2	0.70	0.03	0.003	0.71	0.03	0.003	0.73	0.02	0.002
CN-Ha2	0.87	0.05	0.01	0.86	0.05	0.01	0.83	0.05	0.01
CN-Qia	0.54	0.16	0.03	0.55	0.16	0.03	0.54	0.16	0.03
CN-Din	0.77	0.04	0.003	0.76	0.04	0.003	0.77	0.04	0.003
CN-Cha	0.38	-0.08	0.02	0.39	-0.09	0.02	0.38	-0.08	0.02

Table 5. As in Table 3 but for sensible heat flux.

Site Code	Default			Czil			Newczil		
	R	MBE	RMSE	R	MBE	RMSE	R	MBE	RMSE
CN-Dan	0.54	12.25	663.28	0.54	4.66	340.11	0.54	4.66	340.11
CN-Sw2	0.82	-9.37	508.41	0.83	-9.19	468.04	0.85	-12.21	424.84
CN-Cng	0.74	7.29	442.85	0.75	6.45	387.70	0.73	2.66	274.10
CN-HaM	0.32	-12.03	679.30	0.33	-12.69	597.83	0.33	-13.29	462.76
CN-Du2	0.74	2.57	602.27	0.75	0.87	529.45	0.75	-5.22	461.64
CN-Ha2	0.51	-10.54	905.12	0.56	-13.32	765.79	0.57	-19.20	769.01
CN-Qia	0.73	10.07	391.62	0.70	3.61	242.20	0.73	10.07	391.57
CN-Din	0.65	3.36	213.55	0.57	-2.43	228.10	0.65	3.36	213.55
CN-Cha	0.69	16.06	677.90	0.73	8.56	377.00	0.69	16.06	677.90

Table 6. As in Table 3 but for latent heat flux.

Site Code	Default			Czil			Newczil		
	R	MBE	RMSE	R	MBE	RMSE	R	MBE	RMSE
CN-Dan	0.90	-15.16	770.62	0.92	-14.87	732.86	0.92	-14.87	732.86
CN-Sw2	0.83	-9.63	232.85	0.83	-9.68	233.76	0.83	-9.61	231.80
CN-Cng	0.90	-5.65	212.66	0.91	-5.65	205.26	0.92	-5.74	173.62
CN-HaM	0.93	3.44	169.75	0.93	3.70	169.13	0.93	1.89	121.43
CN-Du2	0.82	-5.54	167.17	0.82	-5.39	163.21	0.83	-5.14	163.64
CN-Ha2	0.90	-10.03	378.07	0.91	-9.08	329.46	0.93	-9.09	282.24
CN-Qia	0.87	5.03	368.81	0.86	4.45	383.47	0.87	5.03	368.83
CN-Din	0.81	6.36	564.07	0.82	6.82	496.01	0.81	6.36	564.06
CN-Cha	0.94	-4.36	144.94	0.94	-1.94	134.29	0.94	-4.36	144.94

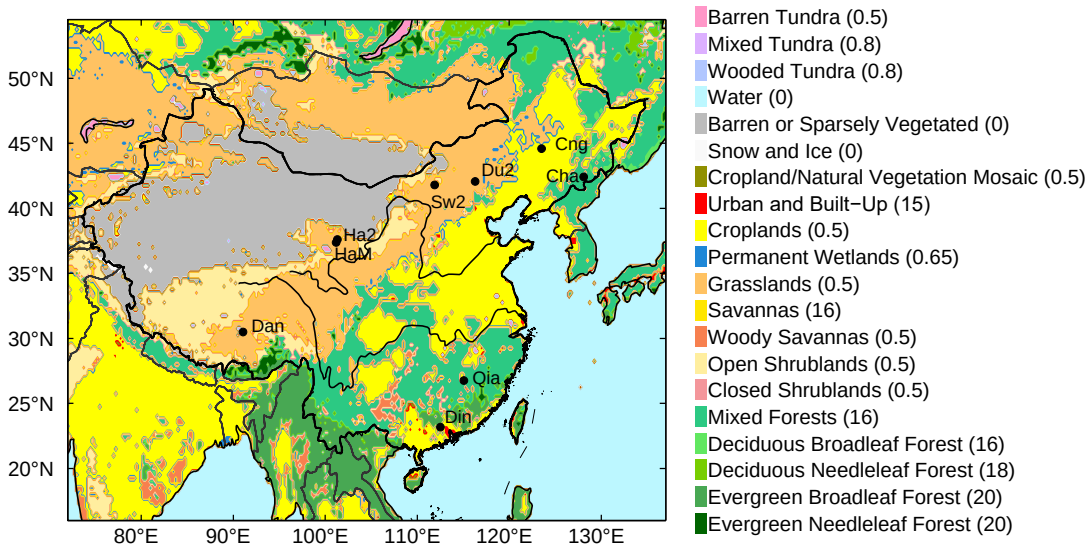

Figure 1. Noah-MP modeling domain and the locations of the nine ChinaFlux sites (dark circles). Shaded contours represent IGBP/MODIS land cover/land use classification. Values in parentheses indicate canopy height (unit: m).

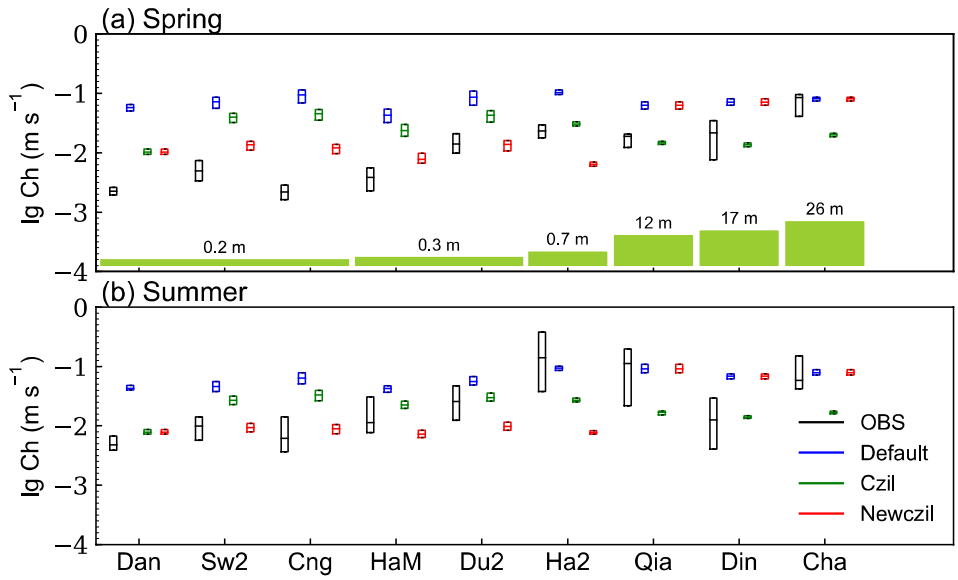

Figure 2. C_h (plotted at log10 scale) derived from the ChinaFlux observations, and calculated by the Noah-MP LSM using the default M-O, C_{zil} = 0.1, and C_{zil}-*h* schemes. These are midday (10:00–15:00 local time) values and averaged for (a) spring and (b) summer. Each box comprises 75% of all midday C_h values for every site, while the middle lines represent the median values of spring (summer) average C_h. Green bars in (a) denote canopy height for each site. Observations are represented by OBS; C_h calculated by the Noah-MP LSM using the default M-O scheme is represented by Default; using the C_{zil} = 0.1 scheme is represented by Czil; and using the C_{zil}-*h* scheme is represented by Newczil.

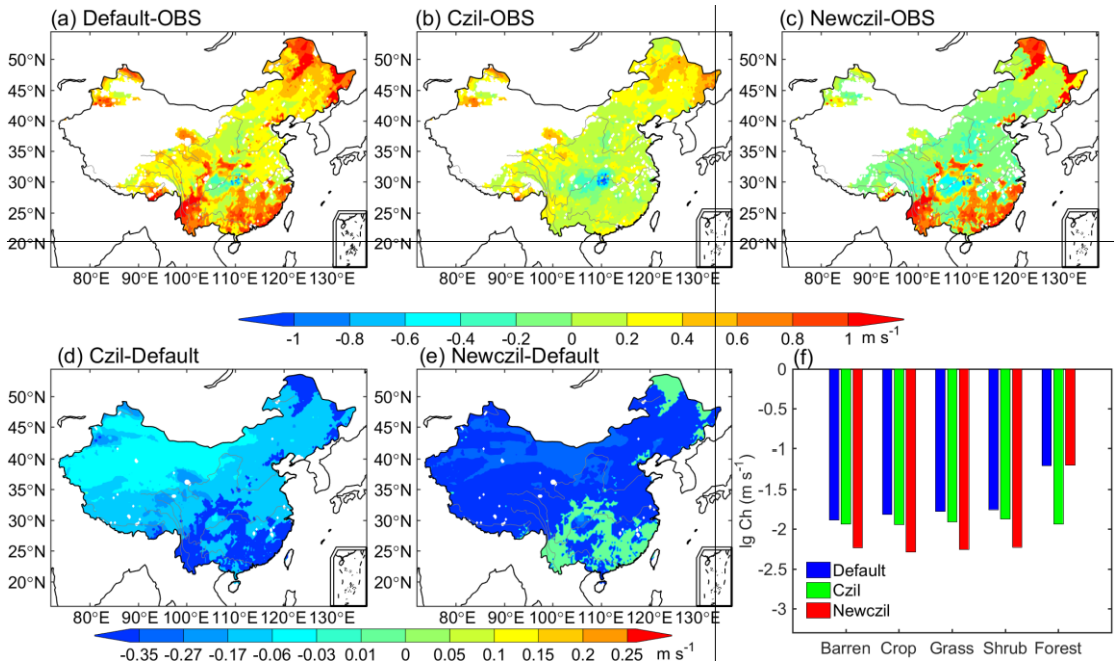

Figure 3. Comparisons of C_h (plotted at log10 scale) over China derived from on-site observations, and calculated by the Noah-MP LSM using the default M-O, C_{zil} = 0.1, and C_{zil}-*h* schemes during the summers of 2003–2012. The differences between the observations and the values simulated by the three schemes are shown in (a)–(c), and the differences between both the C_{zil} = 0.1 and the C_{zil}-*h* schemes and the default M-O scheme are shown in (d) and (e), respectively. Regional averaged C_h values for typical land cover types are shown in (f). The C_h values in (d)–(f) are midday (average of 09:00, 12:00, and 15:00 local time) averages, but those in (a)–(c) are daily averages because only daily observations were available.

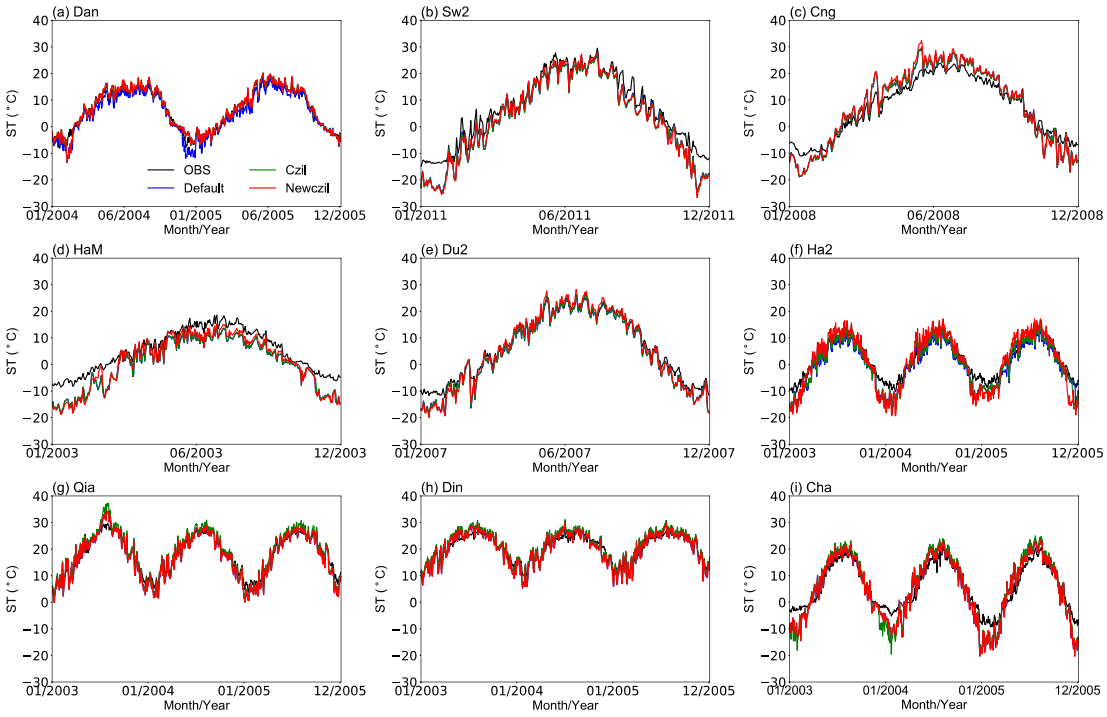

876

877 **Figure 4.** Comparisons of daily average soil temperature (ST) at the depth of 0–10 cm
878 between the ChinaFlux observations and the Noah-MP LSM simulations using the
879 default M-O, C_{zil} = 0.1, and C_{zil}-*h* schemes.
880
881
882
883
884
885
886
887
888
889
890
891
892
893
894
895
896
897
898
899
900

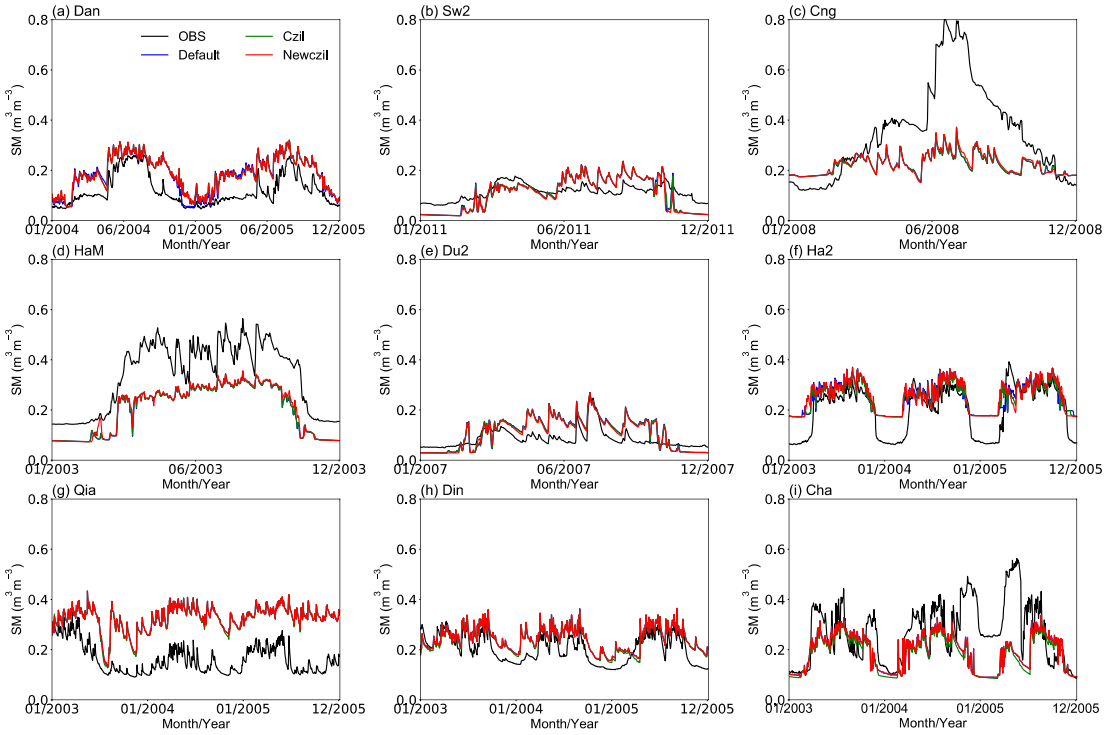

Figure 5. As in Figure 4 but for soil moisture (SM) at the depth of 0–10 cm.

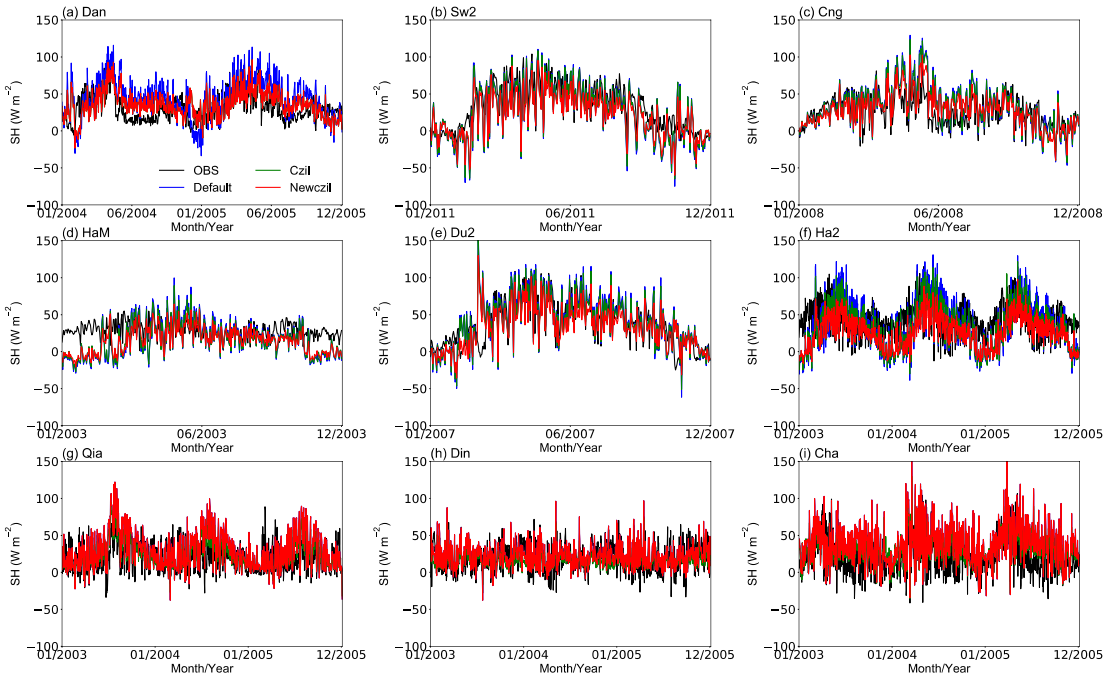

Figure 6. As in Figure 4 but for sensible heat flux (SH).

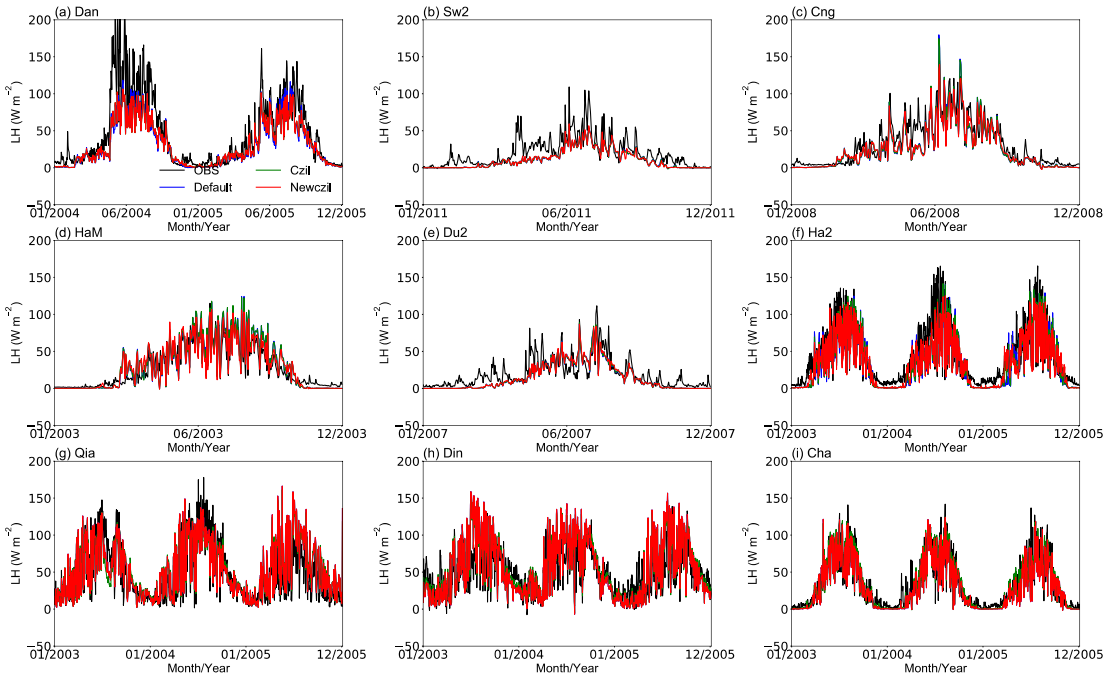

Figure 7. As in Figure 4 but for latent heat flux (LH).

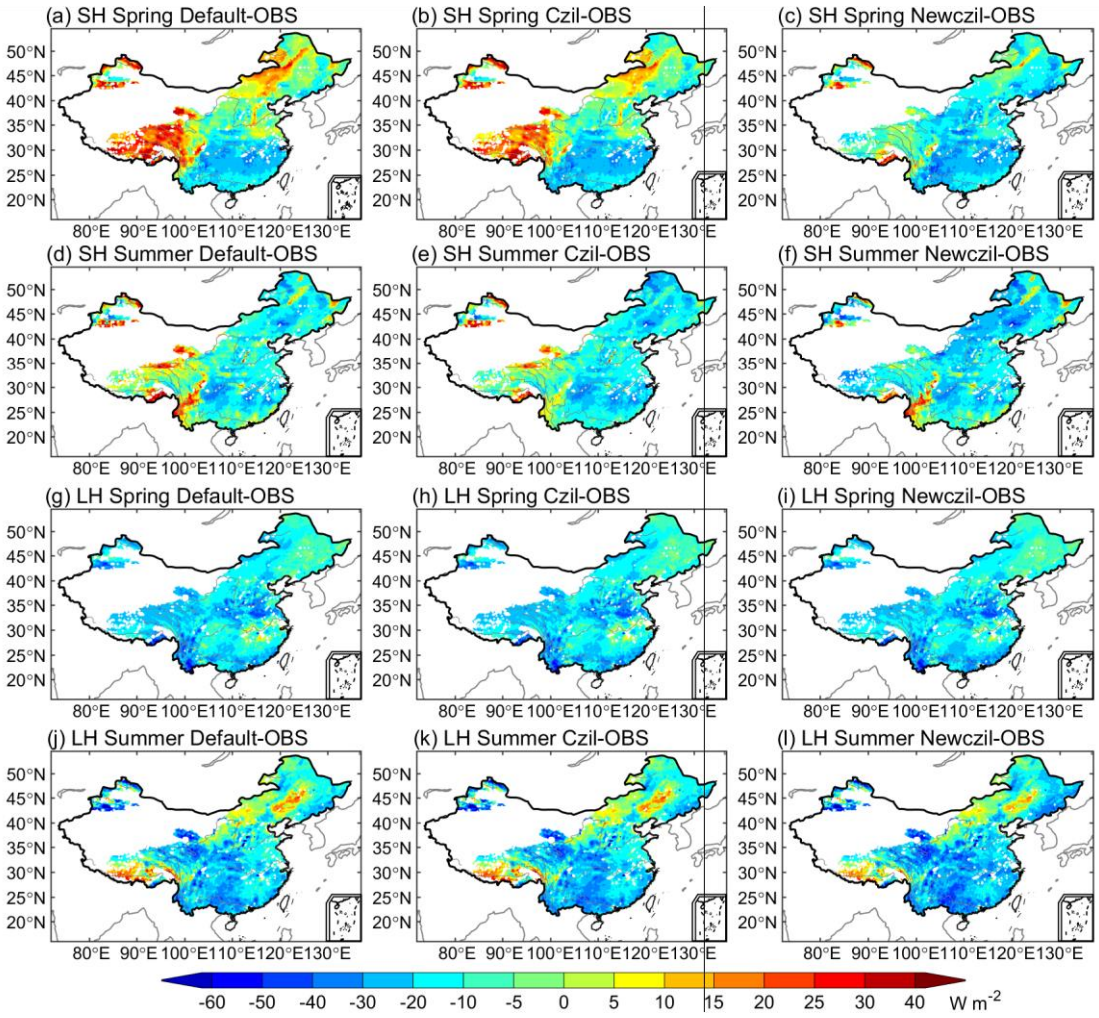

Figure 8. Seasonally spatial differences of LH and SH simulated by the Noah-MP LSM using the default M-O, C_{zil} = 0.1, and C_{zil}-*h* schemes against FLUXNET-MTE observations during spring and summer 2003–2012.

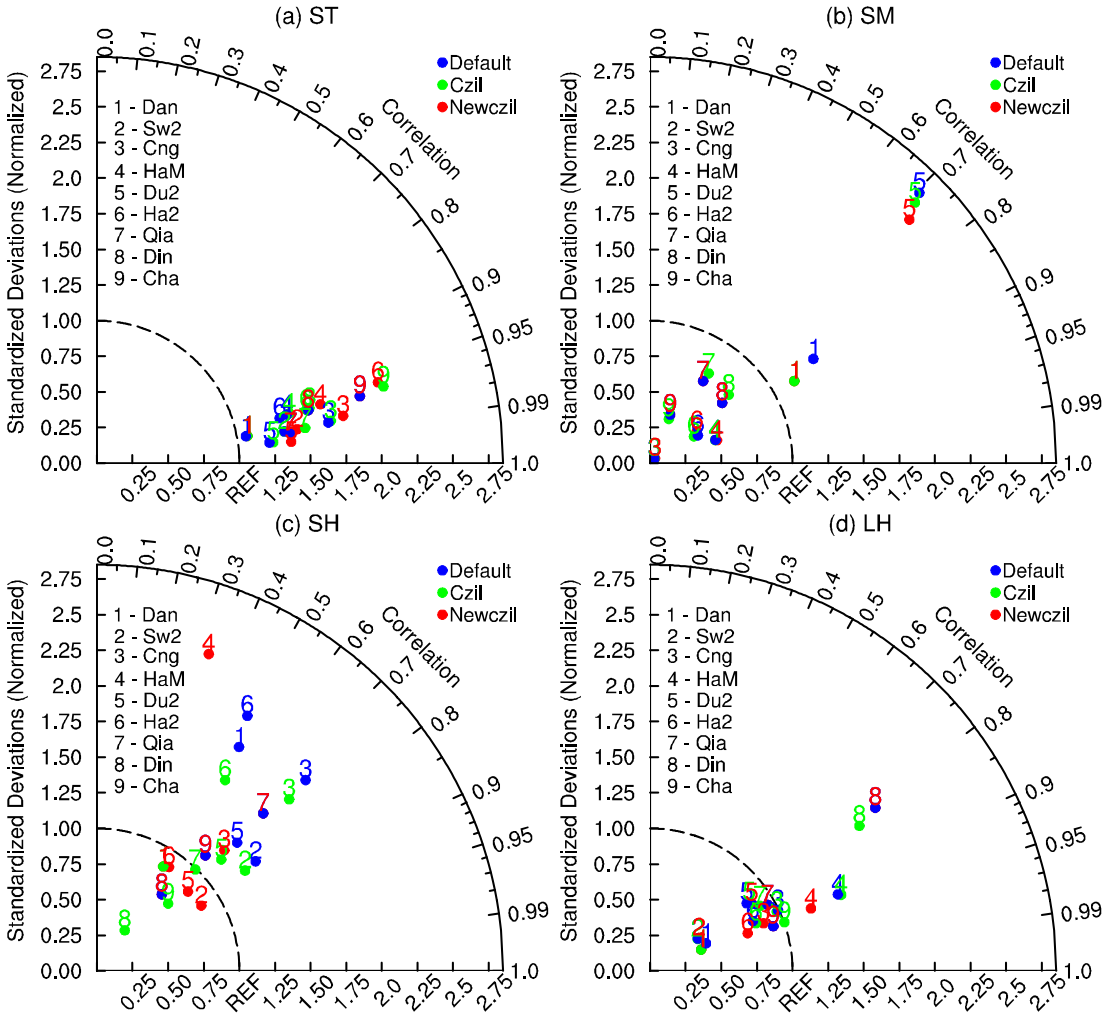

955
956 **Figure 9.** Statistics of daily averaged ST, SM, SH, and LH between the ChinaFlux
957 observations and the Noah-MP LSM simulations using the default M-O, C_{zil} = 0.1, and
958 C_{zil}-*h* schemes. SM and ST are at the depth of 0–10 cm.
959
960
961
962
963
964

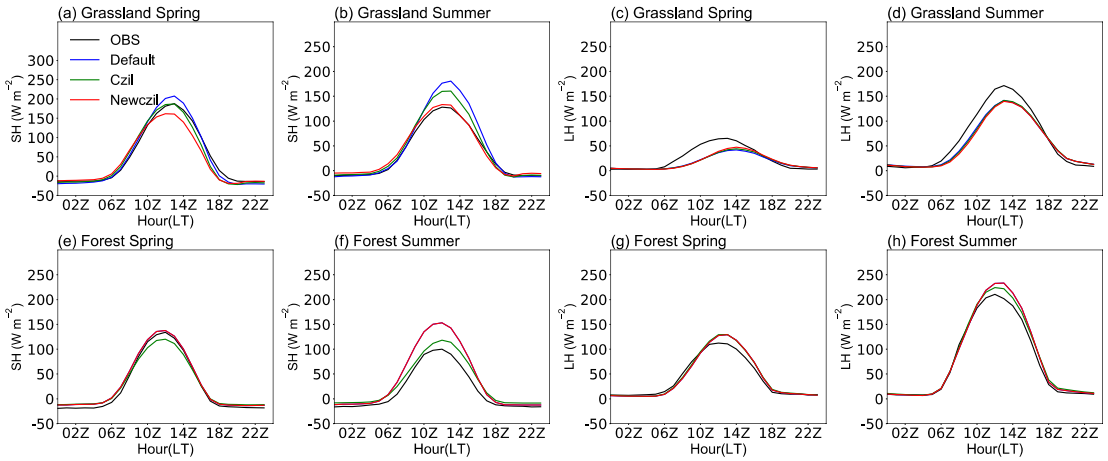

Figure 10. Comparisons of SH and LH between the ChinaFlux observations and the Noah-MP LSM simulations using the default M-O, C_{zil} = 0.1, and C_{zil}-*h* schemes for short and tall vegetation types. The values in (a)–(d) represent short vegetation types averaged from five ChinaFlux grassland sites (Dan, Sw2, Cng, HaM, and Du2), and those in (e)–(h) represent tall vegetation types averaged from three ChinaFlux forest sites (Qia, Din, and Cha).

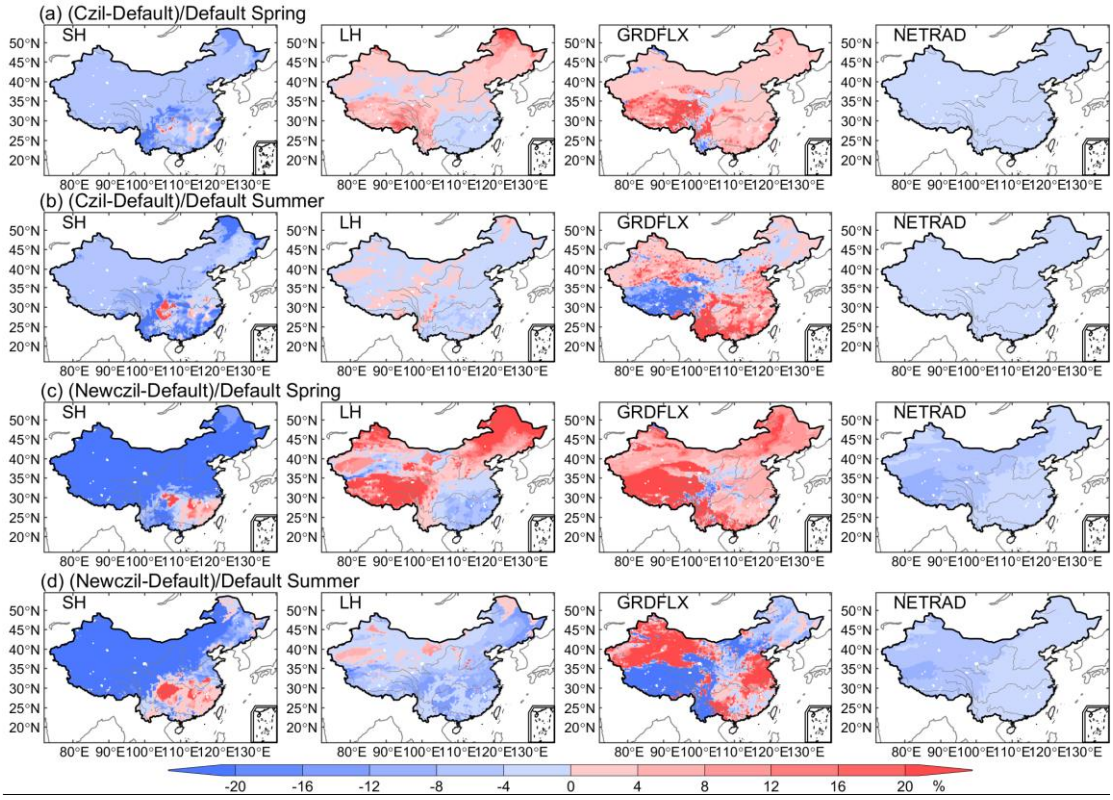

Figure 11. Spatial difference patterns of SH, LH, ground heat flux (GRDFLX), and net radiation (NETRAD) between the C_{zil} = 0.1 and default M-O schemes during spring and summer 2003–2012 are shown in (a) and (b), and the difference patterns between the C_{zil}-*h* and default M-O schemes are shown in (c) and (d).